



Published in final edited form as:

IEEE Trans Med Imaging. 2020 July ; 39(7): 2472–2481. doi:10.1109/TMI.2020.2972200.

## Localization of fluorescent targets in deep tissue with expanded beam illumination for studies of cancer and the brain

**Brian Z. Bentz [Member, IEEE],**

Sandia National Laboratories, Albuquerque, New Mexico 87123, USA

**Sakkarapalayam M. Mahalingam,**

Department of Chemistry, SRM Institute of Science and Technology, Tamil Nadu, India

**Daniel Ysselstein,**

Department of Medicinal Chemistry and Molecular Pharmacology, Purdue University, West Lafayette, IN 47907, USA

**Paola C. Montenegro,**

Department of Medicinal Chemistry and Molecular Pharmacology, Purdue University, West Lafayette, IN 47907, USA

**Jason R. Cannon,**

School of Health Sciences, Purdue University, West Lafayette, IN 47907, USA; Purdue Institute for Integrative Neuroscience, Purdue University, West Lafayette, IN 47907, USA

**Jean-Christophe Rochet,**

Department of Medicinal Chemistry and Molecular Pharmacology, Purdue University, West Lafayette, IN 47907, USA; Purdue Institute for Integrative Neuroscience, Purdue University, West Lafayette, IN 47907, USA

**Philip S. Low,**

Department of Chemistry, Purdue University, West Lafayette, IN 47907, USA

**Kevin J. Webb [Fellow, IEEE]**

School of Electrical and Computer Engineering, Purdue University, West Lafayette, Indiana 47907, USA

### Abstract

Imaging fluorescence through millimeters or centimeters of tissue has important *in vivo* applications, such as guiding surgery and studying the brain. Often, the important information is the location of one of more optical reporters, rather than the specifics of the local geometry, motivating the need for a localization method that provides this information. We present an optimization approach based on a diffusion model for the fast localization of fluorescent inhomogeneities in deep tissue with expanded beam illumination that simplifies the experiment and the reconstruction. We show that the position of a fluorescent inhomogeneity can be estimated while assuming homogeneous tissue parameters and without having to model the excitation profile, reducing the computational burden and improving the utility of the method. We perform

two experiments as a demonstration. First, a tumor in a mouse is localized using a near infrared folate-targeted fluorescent agent (OTL38). This result shows that localization can quickly provide tumor depth information, which could reduce damage to healthy tissue during fluorescence-guided surgery. Second, another near infrared fluorescent agent (ATTO647N) is injected into the brain of a rat, and localized through the intact skull and surface tissue. This result will enable studies of protein aggregation and neuron signaling.

## Keywords

Fluorescence imaging; localization; tumors; brain; turbid media; inverse problems

## I. INTRODUCTION

THERE is substantial interest in imaging fluorescence in deep tissue because it enables studies of targeted biochemical processes in natural environments and *in vivo*. However, such imaging presents a major challenge because the light becomes highly scattered, limiting the information that can be extracted from measurements [1], [2]. Near the tissue surface, microscopy methods such as optical coherence tomography [3] and two-photon microscopy [4] allow imaging at high resolution but with limited depth. Even with feedback control of the amplitude and phase of the incident wavefront, which enables focusing of light through tissue [5], the imaging depth is limited to less than about one millimeter [6]. Imaging at tissue depths beyond one millimeter is achievable with diffuse optical imaging (DOI), where the light propagation is approximated as a diffusion process [7]. In fluorescence diffuse optical tomography (FDOT), a DOI method, computational imaging allows formation of three dimensional (3D) images of optical properties [8]–[10]. FDOT has proven useful for *in vivo* studies in mice and rats, especially when combined with another imaging modality such as CT or MRI to improve spatial resolution [11], [12].

Previously, we have used FDOT and folate-targeted fluorescent contrast agents to image the kidneys and liver in a dead mouse [13] as well as tumors in a live mouse [14]. Our results demonstrated that FDOT is a useful tool for fluorescence guided surgery, where tumor nodules are identified for a surgeon to remove [15]. However, the full volumetric reconstruction performed by FDOT requires extensive computational time, making it ill-suited for an intraoperative environment where real-time imaging is required over a period of hours. Therefore, here we develop an alternative approach using a fast localization method, where only the position of an inhomogeneity is determined. This is accomplished by treating the inhomogeneity as an equivalent point fluorescent source. The position of the point fluorescent source is then estimated through an optimization procedure. We expand upon previous work on localization [16]–[20] by demonstrating that the excitation profile does not need to be modeled and that homogeneous tissue parameters can be assumed to achieve acceptable precision. In this case, the tissue parameters are treated as fitting parameters. We use a mouse model to show that this method can find tumors in deep tissue, and can provide depth information to assist in guided surgery. The near infrared (NIR) folate-targeted molecular contrast agent OTL38 is used in order to computationally localize a tumor in deep tissue [21], [22].

Localization is also valuable for imaging in the brain, where targeted fluorescent agents allow studies of, for example, misfolding of protein aggregates [23] and neuron activation [24], [25]. Modulation of the fluorescence emission in space, time, or wavelength may enable superresolution diffuse optical imaging (SRDOI) through localization of individual fluorescent emitters, providing images with higher resolution than have previously been possible in deep tissue [19]. However, sufficient fluorescent signal must be present to overcome the background tissue autofluorescence. For this reason, we employ ATTO647N, another NIR dye, that is bright for its wavelength and has a long fluorescence lifetime. We demonstrate that localization of a fluorescent inhomogeneity in the brain through the intact head (including the skull) of a rat is possible.

We describe a diffusion model for a point fluorescent source within a highly scattering medium in Section II. This model is used to develop a localization framework to estimate the position of a fluorescent inhomogeneity in Section III, where we make use of the fact that the excitation source does not need to be modeled. We describe the experimental setup in Section IV. The localization of a tumor in a mouse is described in Section V, and the localization of fluorescence in a rat brain is presented in Section VI. We consider applications in Section VII, and conclude in Section VIII.

## II. MODELS

### A. Coupled Diffusion Equations

The diffusion model for describing light transport in highly scattering media is briefly reviewed. In the presence of fluorescence, two coupled diffusion equations are required to model the propagation of photons at the fluorophore excitation wavelength,  $\lambda_x$ , and the fluorophore emission wavelength,  $\lambda_m$ . For  $\exp(j\omega t)$  time variation, where  $\omega$  is the angular modulation frequency, the coupled diffusion equations are [9], [26], [27]

$$\nabla \cdot [D_x(\mathbf{r}) \nabla \phi_x(\mathbf{r}, \omega)] - [\mu_{a_x}(\mathbf{r}) + j\omega/c] \phi_x(\mathbf{r}, \omega) = -S_x(\mathbf{r}; \omega) \quad (1)$$

$$\nabla \cdot [D_m(\mathbf{r}) \nabla \phi_m(\mathbf{r}, \omega)] - [\mu_{a_m}(\mathbf{r}) + j\omega/c] \phi_m(\mathbf{r}, \omega) = -\phi_x(\mathbf{r}, \omega) S_f(\mathbf{r}, \omega), \quad (2)$$

where  $\mathbf{r}$  denotes the position,  $\phi$  (W/mm<sup>2</sup>) is the photon flux density,  $D = 1/[3(\mu'_s + \mu_a)]$  is the diffusion coefficient, with  $\mu_a$  the absorption coefficient (mm<sup>-1</sup>) and  $\mu'_s$  the reduced scattering coefficient (mm<sup>-1</sup>),  $c$  is the speed of light in the medium, the subscripts  $x$  and  $m$  denote parameters at  $\lambda_x$  and  $\lambda_m$ ,  $S_x$  is the excitation source term, and  $S_f$  is the fluorescence source term. Equations (1) and (2) are coupled through the  $\phi_x(\mathbf{r}, \omega)$  term on the right hand side of (2). In an infinite homogeneous space, the diffusion equation Green's function is

$$g(\mathbf{r}', \mathbf{r}) = \frac{e^{-jk|\mathbf{r} - \mathbf{r}'|}}{4\pi|\mathbf{r} - \mathbf{r}'|}, \quad (3)$$

where  $\mathbf{r}'$  is the position of a point source and  $k^2 = -\mu_a/D - j\omega/(Dc)$ , and  $\mu_a$  and  $D$  are determined at  $\lambda_x$  or  $\lambda_m$  for use in (1) and (2), respectively.

## B. Forward Model for Localization

Equations (1) and (2) can be solved on an unstructured finite element method (FEM) mesh [28], [29], useful for general imaging of inhomogeneous media. However, the FEM solution requires extensive computational time, limiting its application in situations where it is important to obtain image information quickly, such as during surgery. For this reason, we adopt a closed-form analytic solution proposed by Milstein *et al.* [16] that assumes an infinite homogeneous domain, enabling fast computation. The geometry is shown in Fig. 1. We assume a general excitation source,  $S_x(\mathbf{r}_s, \omega)$ , is located at  $\mathbf{r}_s$  such that the photon flux density that excites a fluorescent inhomogeneity located at  $\mathbf{r}_f$  is

$$\phi_x(\mathbf{r}_f, \omega) = \int g_x(\mathbf{r}_s, \mathbf{r}_f) S_x(\mathbf{r}_s, \omega) d\mathbf{r}_s, \quad (4)$$

where  $g_x(\mathbf{r}_s, \mathbf{r}_f)$  represents the diffusion equation Green's function for (1) at  $\lambda_x$ . We further assume that  $N$  point detectors at  $\lambda_m$  are located at positions  $\mathbf{r}_i$  where  $i$  is an index from 1 to  $N$ . Finally, we consider a single fluorescence point source is located at  $\mathbf{r}_f$  such that  $S_f(\mathbf{r}, \omega) = \eta_f \mu_{af} \delta(\mathbf{r} - \mathbf{r}_f)$ , where  $\eta_f$  and  $\mu_{af}$  are the quantum yield and absorption of the fluorophore, respectively, and  $\delta$  is the Dirac delta function (with units of  $\text{mm}^{-3}$ ). Estimating  $\mathbf{r}_f$  constitutes localization. The  $i$ th forward model solution  $\tilde{f}_i$  of the fluorescence emission measured at  $\mathbf{r}_i$  is then

$$\tilde{f}_i(\mathbf{r}_f) = w [g_m(\mathbf{r}_f, \mathbf{r}_i) \phi_x(\mathbf{r}_f, \omega)] \quad (5)$$

$$\equiv w f_i(\mathbf{r}_f), \quad (6)$$

where  $w$  is a multiplicative constant that incorporates the quantum efficiency, digital to analog conversion, and solid angle of the detector, the efficiency of light coupling out of the medium (assumed constant for each detector), and  $\eta_f$  and  $\mu_{af} \cdot g_m(\mathbf{r}_f, \mathbf{r}_i)$  is the diffusion equation Green's function for (2) at  $\lambda_m$ . The Green's functions are derived for a semi-infinite medium with a single physical boundary. We set  $\omega = 0$  to correspond to continuous wave (not pulsed or modulated) light. The detectors are modeled as effective isotropic point detectors, and the source and detectors are placed one transport length ( $l^* = 3D$ ) below the physical boundary, as shown in Fig. 1 [16], [19]. An extrapolated zero flux boundary condition is enforced at a distance  $I_s = 5.03D$  above the physical boundary using image sources [26], and analytic expressions for  $g_x(\mathbf{r}_s, \mathbf{r}_f)$  and  $g_m(\mathbf{r}_f, \mathbf{r}_i)$  are found using (3) and subtracting the contributions of the image sources. Considering the coordinate system in Fig. 1 and letting  $\mathbf{r}_i = (x_i, y_i, z_i)$  and  $\mathbf{r}_f = (x_f, y_f, z_f)$ , we find

$$g_m(\mathbf{r}_f, \mathbf{r}_i) = \frac{1}{4\pi} \left[ \frac{e^{-jk r_a}}{r_a} - \frac{e^{-jk r_b}}{r_b} \right], \quad (7)$$

where  $r_a = \left[ (x_i - x_f)^2 + (y_i - y_f)^2 + (z_i - z_f)^2 \right]^{1/2}$  is the distance from the fluorescent source to the detector and  $r_b = \left[ (x_i - x_f)^2 + (y_i - y_f)^2 + (-z_i + z_f - 6D - 2l_s)^2 \right]^{1/2}$  is the distance from the image fluorescent source to the detector.

### III. LOCALIZATION WITH EXPANDED BEAM ILLUMINATION

If a fluorescent inhomogeneity is present, its position can be estimated by finding the value of  $\mathbf{r}_f$  that minimizes the cost function [16]

$$c(\mathbf{r}_f) = \min_w \|\mathbf{y} - w\mathbf{f}(\mathbf{r}_f)\|_{\mathbf{Y}^{-1}}^2, \quad (8)$$

where  $\mathbf{y}$  is a vector of  $N$  measurements,  $\mathbf{f}(\mathbf{r}_f)$  is a vector of  $N$  forward calculations  $f_i(\mathbf{r}_f)$  from (6),  $\mathbf{Y} = \alpha \text{diag}[|y_1|, \dots, |y_N|]$  is the noise covariance matrix, for which we assume a shot noise model characterized by  $\alpha$  [30], and, for an arbitrary vector  $\mathbf{v}$ ,  $\|\mathbf{v}\|_{\mathbf{Y}^{-1}}^2 = \mathbf{v}^H \mathbf{Y}^{-1} \mathbf{v}$ , where  $H$  denotes the Hermitian transpose. We consider the case where a single excitation source is present at position  $\mathbf{r}_s$ . Therefore, the measurements will have a linear dependence on  $\phi_x(\mathbf{r}_f, \omega)$ , allowing (8) to be written

$$c(\mathbf{r}_f) = \min_w \|\mathbf{y} - w\phi_x(\mathbf{r}_f, \omega)\mathbf{h}(\mathbf{r}_f)\|_{\mathbf{Y}^{-1}}^2, \quad (9)$$

where  $h_i(\mathbf{r}_f) = g_m(\mathbf{r}_f, \mathbf{r}_i)$  is the  $i$ th component of  $\mathbf{h}(\mathbf{r}_f)$ . In general, calculating  $\phi_x(\mathbf{r}_f, \omega)$  is important for simulating the correct fluorescence emission distribution within the medium. However, because of the linear dependence,  $\phi_x(\mathbf{r}_f, \omega)$  can be incorporated into a new multiplicative constant,  $w_s$ , as

$$c(\mathbf{r}_f) = \min_{w_s} \|\mathbf{y} - w_s\mathbf{h}(\mathbf{r}_f)\|_{\mathbf{Y}^{-1}}^2. \quad (10)$$

If the measurement is not linear in  $\phi_x(\mathbf{r}_f, \omega)$ , as would be the case when multiple fluorescent sources are present and in FDOT,  $\phi_x(\mathbf{r}_f, \omega)$  cannot be incorporated into  $w_s$ .

For localization, our goal now is to find the  $\mathbf{r}_f$  that minimizes (10), and we note that the inverse problem is linear in  $w_s$  and nonlinear in  $\mathbf{r}_f$ . Equation (10) can be minimized using a two step procedure [16]. First, we set the derivative of  $\|\mathbf{y} - w_s\mathbf{h}(\mathbf{r}_f)\|_{\mathbf{Y}^{-1}}^2$  with respect to  $w_s$  equal to zero and solve for  $w_s$ , resulting in

$$\tilde{w}_s(\mathbf{r}_f) = \frac{\mathbf{h}^T(\mathbf{r}_f)\mathbf{Y}^{-1}\mathbf{y}}{\mathbf{h}^T(\mathbf{r}_f)\mathbf{Y}^{-1}\mathbf{h}(\mathbf{r}_f)}, \quad (11)$$

$$c(\mathbf{r}_f) = \|\mathbf{y} - \tilde{w}_s(\mathbf{r}_f)\mathbf{h}(\mathbf{r}_f)\|_{\mathbf{Y}^{-1}}^2. \quad (12)$$

Second, we calculate (12) at a set of positions  $\mathbf{r}_f$  within a region of interest that encompasses the true location. The maximum likelihood estimates are then

$$\hat{\mathbf{r}}_f = \underset{\mathbf{r}_f}{\operatorname{argmin}} c(\mathbf{r}_f), \quad (13)$$

$$\hat{w}_s = \hat{w}_s(\hat{\mathbf{r}}_f). \quad (14)$$

An important step in our derivation that differentiates it from the method developed by Milstein *et al.* [16] is the incorporation of  $\phi_x(\mathbf{r}_f, \omega)$  into  $w_s$ . This step implies that the inverse problem can be solved without consideration or modeling of the excitation source because  $\phi_x(\mathbf{r}_f, \omega)$  does not need to be computed. This is of great utility because complicated illumination patterns (such as an expanded beam) do not need to be modeled.

We demonstrate localization of a fluorescent inhomogeneity numerically in Fig. 2, and show that minimizing (12) without modeling the excitation source is equivalent to minimizing (8) and modeling the excitation source. Figure 2(a) shows the simulation geometry, where 25 point detectors (blue) and 1 point excitation source (red) are placed at the  $z = 10$  mm plane, and a fluorescent point source (green) is located at  $\mathbf{r}_f = (5.0, 5.0, 5.0)$  mm. Simulated measurement data  $\mathbf{y}$  was generated using (6) (which included modeling of a point excitation source through calculation of  $g_x(\mathbf{r}_s, \mathbf{r}_f)$ ) and adding shot noise with an assumed 30 dB SNR [30]. The  $10 \text{ mm} \times 10 \text{ mm} \times 10 \text{ mm}$  volume below the detectors was defined as the region of interest and discretized into a Cartesian grid. Equations (12) and (8) were then calculated at each grid point, and the grid point with the minimum cost is  $\hat{\mathbf{r}}_f$ , according to (13). Figure 2(b) plots the normalized cost function calculated as a function of position,  $x$ , for  $x_f = 2, 5$ , and  $8$  mm, as indicated by the legend, and fixed  $y_f = 5.0$  mm and  $z_f = 5.0$  mm. The circular markers signify cost calculations using (8), and the solid lines signify cost calculations using (12). We see that both cost functions are the same after being normalized to their maximum, demonstrating that  $g_x(\mathbf{r}_s, \mathbf{r}_f)$  can be incorporated into  $w_s$  and does not need to be calculated for the inversion. Both cost functions have a single minimum at the same value of  $x = 4.52$  mm.

## IV. EXPERIMENTS

We present two applications of localizing fluorescent inhomogeneities. The first is finding folate-targeted fluorescent agents to assist in guided surgery, and the second is localization of an inhomogeneity in the brain. Both applications use the same experimental setup, which is described in this section.

### A. Experimental Setup

The experimental setup is similar to what we have used previously for FDOT [31], and a schematic is shown in Fig. 3. Laser excitation light at  $\lambda_x$  is reflected through a beam expander onto the surface of the subject (shown in Fig. 3 as a mouse). We used a microscope objective with a short focal length as the beam expander. The output of a pulsed supercontinuum source (EXR-20 NKT Photonics, 5 ps seed pulse width, 20 MHz repetition

rate) is filtered by a VARIA tunable filter to generate excitation light at a desired wavelength and bandwidth. With a typical 10 nm bandwidth, the average power is about 15 mW. Light at  $\lambda_m$  is emitted from fluorophores in deep tissue (green circle), reflected from a mirror, and detected by a CCD camera (PIMAX,  $512 \times 512$  pixels) through an emission bandpass filter centered at  $\lambda_m$ . A f/2.8 camera lens (AF micro Nikkor, Nikon) was focused to the surface of the subject. All measurements were pseudo-CW, where the CCD camera integration time was much longer than the inverse of the pulsed laser repetition rate (50 ns). A 3D topography laser line scanner (not shown in Fig. 3) was employed to obtain the 3D profile of the subject [13]. The 3D profile was used to determine the detector positions by projecting the CCD camera pixels to the subject's surface [32]. The 3D topography scanner was controlled using a 150 mm motorized linear stage (Zaber T-LSM150A-KT04U). From Fig. 1, the simulated detectors are each placed  $z = -3D$  below the boundary. Considering (7), the simulated fluorescence image source is placed along the  $z$  dimension and above the physical boundary. We have therefore assumed that the  $z$  direction is approximately normal to the tissue surface, removing the need to calculate surface normal vectors. This forward model solution is calculated for each simulated detector position  $\mathbf{r}_j = (x_j, y_j, z_j)$ . Then, for each detector, a different zero-flux boundary condition is satisfied at approximately  $z = l_s$  above the local tissue surface.

## V. TUMOR LOCALIZATION

Over forty percent of human cancer cells over-express folate receptors, enabling the cells to be identified using folate-targeted fluorescence imaging [33], [34]. In a typical study, a fluorophore is attached to the targeting agent (folate) and injected into the blood stream of an animal. The fluorescent agent is then distributed to the extracellular extravascular space, where it is either captured by a folate receptor and retained in the receptor-expressing (cancer) tissue or is rapidly cleared from receptor-negative (healthy) tissues and excreted from the body [35]. Roughly 30 minutes after injection, the fluorescent agent is mostly cleared from the blood, and is concentrated in the kidneys, the liver, and any tumors that are present (the fluorescent agent is present in the kidneys and liver because these organs constitute the major routes of excretion of the fluorescent dye). This process introduces a contrast in fluorescence throughout the tissue, enabling fluorescence-guided surgery. In a previous study, it was shown that a surgeon can detect 5 times more malignant masses with the aid of fluorescence than with the naked eye [34]. However, once a tumor has been identified, additional information about its location, such as its depth, could be used to minimize damage to the surrounding healthy tissue. Here, we use a mouse model to demonstrate that the location of a tumor can be estimated using our localization method. Expanded beams are commonly used for illumination in fluorescence-guided surgery, further motivating the development of our approach.

Female nu/nu mice purchased from NCI Charles River Laboratories were maintained on folate deficient rodent chow for 3 weeks prior to experimental study and kept on a standard 12 hour light-dark cycle. The animal procedure was carried out with the approval of the Purdue Animal Care and Use Committee in accordance with NIH guidelines. Tumor cells ( $10^6$  of L1210A) were injected intravenously into the tail vein of a six-week-old female nu/nu mouse. The cancer cells were allowed to grow for 30 days, at which point 10 nmol of



a folate-targeted fluorescent agent (OTL38) dissolved in saline was injected intravenously via the tail vein. The OTL38 attached itself to the folate-receptors present in the tumors, allowing for fluorescent imaging [21], [22]. Two hours after injection of OTL38, the mouse was euthanized through CO<sub>2</sub> asphyxiation. The mouse was then placed on its side in the experimental setup shown in Fig. 3.

OTL38 is a tumor-targeted near infrared fluorescent dye comprised of folic acid linked to an indocyanine fluorophore. The peak excitation of the OTL38 is 770 nm and the peak emission is 790 nm. The lower absorption and scattering of light in tissue at these wavelengths relative to shorter wavelengths enables deep tissue imaging. An OD4 emission bandpass filter with a center wavelength of 780 nm and a 10 nm bandwidth (Andover - 780FS10-50) was placed in front of the CCD camera in order to measure the fluorescence emission. The wavelength of the expanded-beam excitation light from the EXR-20 was tuned by the VARIA until peak emission and low filter bleed through were observed. This procedure resulted in an excitation wavelength of 740 nm with a 10 nm bandwidth.

The 3D topography of the mouse was captured using the laser line scanner. Laser light was focused through a cylindrical lens to form a line, which was scanned along the length of the mouse to 92 positions. At each position, a CCD camera image was captured. Figure 4(a) shows one of these 92 images. The line scans were combined and calibrated using the corresponding scans of a half-cylinder [13] in order to form the 3D mouse topography shown in Fig. 4(b). This 3D topography was used to determine the positions of CCD pixels on the surface of the mouse, giving  $\mathbf{r}_f$ . Figure 4(c) shows a fluorescence image of a portion of the mouse captured by the CCD camera through the bandpass filter. Strong fluorescence (in red) from a tumor is clearly visible, as well as fluorescence from the kidney (yellow) and some tissue autofluorescence (cyan). Overlaid on Fig. 4(c) are 144 detectors (red points) that were chosen in the region above a tumor, as well as the line scans used to determine the positions of the detectors (green lines). The values shown by the colorbar (AU) at these 144 detectors form the data vector  $\mathbf{y}$ .

### A. Tumor Localization Results

Localization of the tumor requires that the  $\mu'_s$  and  $\mu_a$  of the tissue are known so that  $g_m(\mathbf{r}_f, \mathbf{r}_j)$  can be calculated using (3) subject to the boundary condition. The  $\mu'_s$  and  $\mu_a$  can be determined from the literature [36], or they can be estimated by incorporating them into the optimization problem. We chose to estimate  $\mu_a$  in order to improve the accuracy of the localization. This was accomplished by fixing  $\mu'_s = 1.6 \text{ mm}^{-1}$  [13], and, for each  $\mathbf{r}_f$  within the region of interest, calculating the cost in (12) for values of  $\mu_a$  between 0 and  $0.05 \text{ mm}^{-1}$  separated by increments of  $0.005 \text{ mm}^{-1}$ . The position of the fluorescent inhomogeneity was then estimated as the position  $\mathbf{r}_f$  that minimized the cost in (12). Because the tissue is inhomogeneous and our model assumes that it is homogeneous, estimated values of  $\mu_a$  and  $\mu'_s$  represent effective values obtained from a fitting procedure. For localization, we are only interested in the position of the inhomogeneity.

The results of this localization procedure using data from Fig. 4 are presented in Fig. 5. The region of interest was defined as a Cartesian grid confined by the mouse 3D topography of



Fig. 4(b). The position that minimized (12), or the estimated position of the tumor, was (11.1, 17.0, 9.0) mm, a reasonable result given the location of the fluorescence intensity at the tissue surface in Fig. 4(c). Figures 5(a) and (b) show flat field images of the cost function for 2D slices at  $y = 17$  mm and  $z = 9$  mm, respectively. Figure 5(c) shows a plot of the node boundary in green obtained using the 3D topography laser line scan, the simulated detector positions in blue, and the estimated tumor location in red. The depth of the tumor was estimated to be about 6.4 mm. In Fig. 5(d), the measured data vector  $\mathbf{y}$  from Fig. 4(c) is plotted with the estimated  $\mathbf{y}$ , or  $\hat{\mathbf{y}} = \hat{\mathbf{w}}_s \mathbf{h}(\mathbf{r}_f)$ . Since the surface is slowly varying, and only one inhomogeneity dominates the contribution to the data at the detectors, the model fits the data well. The discrepancy could be due to autofluorescence, fluorescence from the kidney, errors in the 3D topography, or assumptions made in the forward model derivation.

The localization method was implemented in MATLAB and run on a 12 core computer with 3.47 GHz Intel X5690 processors and 96 GB RAM. In order to improve the computational time, the MATLAB parallel computing toolbox [37] was used to distribute computation of the cost function across multiple processors. Subsets of the set of nodes within the region of interest were assigned to each processor so that the cost could be calculated at each node position. Without parallel processing, the computational time for the results in Fig. 5 was 30.9 minutes. With parallel processing, the computational time was reduced to 3.3 minutes, which is much more manageable for applications in surgery, but insufficient for live intervention. The computational time could be further reduced, for example, by decreasing the number of nodes within the region of interest or reducing the number of detectors. The number of nodes could be reduced significantly using the multiresolution method that we have described previously, potentially offering at least a factor of 10 reduction in computational time [19], [20].

## VI. BRAIN LOCALIZATION

Essential to *in vivo* studies of the brain is the ability to detect fluorescence from deep in the tissue. This is a difficult task because the fluorescent signal is highly attenuated on its way to the surface by the high  $\mu_a$  and  $\mu'_s$  of brain tissue [36]. However, here we demonstrate that with a sufficient concentration of NIR dye, fluorescent signals can be detected from deep within the brain, opening the door for important optical imaging studies.

We chose to use the dye ATTO647N because its optical properties are amenable to *in vivo* imaging. Namely, its peak excitation and emission wavelengths are 646 nm and 664 nm, respectively. Thus, there is expected to be far less interference from biomolecules with absorbing properties at shorter wavelengths. An OD6 emission bandpass filter centered at 676 nm with a 29 nm bandwidth (Edmund Optics - 86-996) was used to measure the fluorescence emission. The dye was excited by the expanded light from the EXR-20 filtered to 633 nm with a 10 nm bandwidth. The dye is bright for its wavelength, with a quantum yield of 0.65 and a fluorescence lifetime of 3.5 ns. A 10 mM stock solution of 1 mg maleimide ATTO647N (868 g/mol) and 115  $\mu\text{L}$  of PBS was prepared. The stock solution was used to form 50  $\mu\text{L}$  aliquots at concentrations of 10 mM, 1 mM, and 0.1 mM, as shown in Fig. 6(a). We found significant quenching at high concentration, as seen in Fig. 6(b) [38].

For this reason, 2  $\mu\text{L}$  of the 1 mM solution was used for stereotaxic injections, as shown in Fig. 6(c).

In order to study the signal level, CCD fluorescence images of a rat were captured before and after injection of ATTO647N. The rat was euthanized (before injection) and handled in accordance with the Purdue animal care and use committee (PACUC) guidelines. It was shaved in order to reduce autofluorescence and scattering. First, the top of the rat was imaged, as shown in Figs. 7(a) and (b). Next, the 2  $\mu\text{L}$  solution of ATTO647N was stereotaxically injected into the *substantia nigra* (8 mm below the surface of the skull) at a rate of 2 nL/sec. After injection the needle was kept in place for 10 minutes before being slowly removed. The tissue was sutured and washed, and the top of the rat was imaged again, as shown in Figs. 7(c) and (d). A strong fluorescence signal is visible above the injection site. The same signal was observed after pinching the skin and shifting it, ensuring that the signal emanated from deep within the brain and not from near the tissue surface. This result demonstrates that it is possible to detect fluorescent inhomogeneities within the brain for *in vivo* studies of, for example, the rat *substantia nigra*.

### A. Brain Localization Results

The injected ATTO647N was localized with the same method that was used to find the tumor in Section V-A. The assumption of an infinite homogeneous medium and the use of parallel computing enabled fast computation. The 3D topography of the rat shown in Fig. 8(a) was used to define a region of interest and place 104 detectors in the region above the injection site. The scatter was fixed at  $\mu'_s = 2.0 \text{ mm}^{-1}$  [36], and  $\mu_a$  was ranged from  $0.02 \text{ mm}^{-1}$  to  $0.05 \text{ mm}^{-1}$  in increments of  $0.005 \text{ mm}^{-1}$ . As in Section V-A, the cost was calculated for each  $\mu_a$  within the range at all nodes within the region of interest. The results of the localization are presented in Fig. 8(b)–(e). The position that minimized the cost was (19.8, 16.6, 24.0) mm (with  $\mu_a = 0.025 \text{ mm}^{-1}$ ), giving an estimated depth of about 8.3 mm below the tissue surface, which is close to the injection depth (8 mm below the skull). Figures 8(b) and (c) show flat field images of the cost function for 2D slices at  $y = 17 \text{ mm}$  and  $z = 24 \text{ mm}$ , respectively. Figure 8(d) shows a plot of the node boundary in green obtained using the 3D topography laser line scan and the estimated fluorescent source location in red. In Fig. 8(e), the measured data vector  $\mathbf{y}$  is plotted with the estimated  $\hat{\mathbf{y}} = \hat{\mathbf{w}}_s \mathbf{h}(\hat{\mathbf{r}}_f)$ . The surface is not as slowly varying as that of Fig 4, and there is significant autofluorescence, causing errors in the fit. However, it was still possible to estimate the correct depth of the ATTO647N.

## VII. DISCUSSION

We have developed an approach for the localization of a fluorescent source in deep tissue. The primary innovation of the method is the incorporation of the excitation flux into a linear constant, and by optimizing for this quantity, removing the need to model the excitation profile. In principle, this allows an arbitrary illumination profile to be used as long as a single equivalent fluorescent point source is excited, which simplifies the experimental setup. The method's computational time can be short because few detectors are required, the forward model is a closed-form analytical equation, and the calculation of the cost can be distributed between multiple processors. The computational time could be further improved

through implementation of multiresolution methods [19], [20], [39] or potentially through iterative inversion.

We have demonstrated that simple homogeneous analytic solutions to the diffusion equation can be sufficient to localize fluorescent sources in tissue. This could be because the point fluorescent source assumption sufficiently constrains the solution space of the inverse problem such that perturbations due to heterogeneous tissues have a minimal effect on the estimated position. In this case, the estimated tissue parameters are not quantitative and are treated as fitting parameters. However, a FEM or Monte Carlo (MC) solution would provide a better model of the light propagation [40], likely improving the localization accuracy, especially with the incorporation of prior information from another imaging modality [41]. The FEM or MC solution could be used with the same cost function, (10), removing the need to model the excitation source if only a single fluorescent source is present. The FEM or MC solution requires substantial computational time compared to the analytic solutions used here, but it could be precomputed for medical applications. The experiment could be improved by increasing the excitation laser power, which is possible because the light is distributed over a wide area, causing minimal tissue damage. In addition to extracting the location of an inhomogeneity, the localization methods could be modified to extract other parameters of interest, such as kinetic rates or fluorescent lifetimes, which can characterize a model of time-dependent fluorescence [14]. The localization methods could also be used to localize absorption or scattering inhomogeneities [17], [18], provide prior information for FDOT in order to improve reconstructions [16], or implemented with photo-acoustic models [42]. In the case where multiple fluorescent sources are present in the tissue, as long as a set of detectors can be selected for each respective source that measure emission from only that source, the method can be applied sequentially to localize each source. In general, any fluorophore could be used as long as an appropriate optical filter and detector are available at the emission wavelength.

We presented two potential applications of localization. The first was localization of tumors using folate-targeted fluorescent indicators in order to assist with fluorescence-guided surgery. Armed with knowledge of the location of a tumor, a surgeon could perform minimally-invasive surgery in order to remove it, reducing the damage to healthy tissue [43]. The experimental setup in Fig. 3 could be made into a portable imaging device for the clinic and modified to use more sensitive detectors, such as a fiber array. The 3D topography could be measured with the laser line scan or related methods [44], or the tissue surface could be approximated as planar at the expense of reduced localization accuracy.

The second application that we presented was localization of fluorescent indicators in the brain. Optical imaging through the intact skull is a major challenge that requires bright fluorophores, such as ATTO647N. However, the potential applications are far-reaching. For example, *in vivo* imaging of protein aggregation, a leading candidate for the basis and onset of neurological diseases [45], could be pursued. Different aggregation states can modulate fluorescence emission and lifetime [46], [47], and this information could be combined with the localization methods presented here [48] to track the evolution of protein aggregation in a rat disease model [49].

Additionally, the prospect of imaging calcium sensitive dyes to monitor activity of neurons in the brain is of particular interest. Signaling between neurons is accompanied by an increase in the local concentration of calcium, which can modulate fluorescence emission [24], [25]. In principle, measurements with a CCD camera or a fiber array with short integration times could provide data from individual neurons such that each could be localized, providing an image of a whole animal brain *in vivo*. These images of the whole brain could be used to form correlation maps, which are useful for studying neurological diseases and developing treatments [50]. It is likely that an expanded beam illumination profile and fast computation will be required in order to localize many neurons. This type of imaging could provide new information on chemical and electrical neural activity because available *in vivo* methods, such as fMRI [51], provide only indirect access to neurons by measuring secondary parameters.

## VIII. CONCLUSION

We have presented an approach for the localization of fluorescent inhomogeneities in deep tissue that does not require modeling of the excitation profile. The method was demonstrated using a single mouse and a single rat as a proof of concept study. The uncertainty in the estimated position has been shown to be tens of microns in a previous phantom study [19], and future work will involve demonstrating this in live mice and rats.

## Acknowledgment

Brian Z. Bentz is with Sandia National Laboratories. Sandia National Laboratories is a multimission laboratory managed and operated by National Technology and Engineering Solutions of Sandia, LLC, a wholly owned subsidiary of Honeywell International Inc., for the U.S. Department of Energy's National Nuclear Security Administration under contract DE-NA0003525. This paper describes objective technical results and analysis. Any subjective views or opinions that might be expressed in the paper do not necessarily represent the views of the U.S. Department of Energy or the United States Government.

The authors would like to acknowledge funding through the National Science Foundation (CISE-1618908) and the National Institutes of Health (5R21CA182235-02 and 5R21NS105048-02).

## Biographies



**Brian Z. Bentz** received his B.S. and Ph.D. in 2011 and 2017, respectively, from Purdue University, West Lafayette, Indiana, both in electrical and computer engineering. He was a Research Assistant with the Department of Electrical and Computer Engineering at Purdue University from 2012 to 2017. In 2017, he joined the staff at Sandia National Laboratories. He is a member of IEEE, OSA, and APS.



**Sakkarapalayam M. Mahalingam** is an Associate Professor in the Department of Chemistry at SRM Institute of Science and Technology, Tamil Nadu, India. Prior to this, he was an Assistant Research Scientist with the Department of Chemistry and Center for Drug Discovery at Purdue University, West Lafayette, USA from 2013 to 2018. He received his Ph.D. in 2007 from Indian Institute of Technology Madras, Tamil Nadu, India and M.Sc. in 2001 from University of Madras, Tamil Nadu, India and B.Sc. in 1999 from Gobi Arts and Science College (Bharathiar University), Gobichettipalayam, Tamil Nadu, India. His research focuses on developing affordable healthcare technologies based on targeted diagnostics and therapies for cancer and inflammatory diseases.



**Daniel Ysselstein** received his B.S. in biology in 2010 from Calvin College and his Ph.D. in Medicinal Chemistry and Molecular Pharmacology in 2016 from Purdue University. He is currently a Postdoctoral Researcher in the Feinburg School of Medicine at Northwestern University, Chicago Illinois.



**Paola C. Montenegro Larrea** is currently a postdoctoral fellow at Harvard Medical School in Boston, Massachusetts. She received her undergraduate certificate in Biological Sciences from the Pontificia Universidad Catlica del Ecuador (PUCE). She holds a M.Sc. in Molecular Genetics and Diagnostics from The University of Nottingham, UK, and a Ph.D. in Interdisciplinary Life Sciences from Purdue University in West Lafayette, Indiana, USA. Her studies are focused on the characterization of *in vivo* and *in vitro* models that allow the study of Alzheimer's and Parkinson's diseases.



**Jason R. Cannon** is an Associate Professor of Toxicology at Purdue University, West Lafayette, Indiana where he has been on the faculty since 2012. Prior to this, he was a

postdoctoral fellow at the University of Pittsburgh. He received a Ph.D. from the University of Michigan and a B.S. from Michigan State University.



**Jean-Christophe Rochet** is the director of the Purdue Institute for Integrative Neuroscience and a Professor in the Department of Medicinal Chemistry and Molecular Pharmacology at Purdue University, West Lafayette, Indiana, where he has been on the faculty since 2002. Prior to this, he was a postdoctoral fellow at Brigham and Women's Hospital and Harvard Medical School, in Boston, Massachusetts. He received B.S. and Ph.D. degrees from the University of Alberta in Edmonton, Canada.



**Philip S. Low** is the Presidential Scholar for Drug Discovery and Ralph C. Corley Distinguished Professor in the Department of Chemistry at Purdue University, West Lafayette, Indiana, where he has been on the faculty since 1976. He received his B.S. in Chemistry from Brigham Young University and his Ph.D. from the University of California San Diego.



**Kevin J. Webb** is a professor in the School of Electrical and Computer Engineering at Purdue University, West Lafayette, Indiana, where he has been on the faculty since 1990. Prior to this, he was on the faculty of the University of Maryland, College Park, following completion of his Ph.D. at the University of Illinois, Urbana-Champaign, in 1984. He is a Fellow of the IEEE, the OSA, and APS.

## REFERENCES

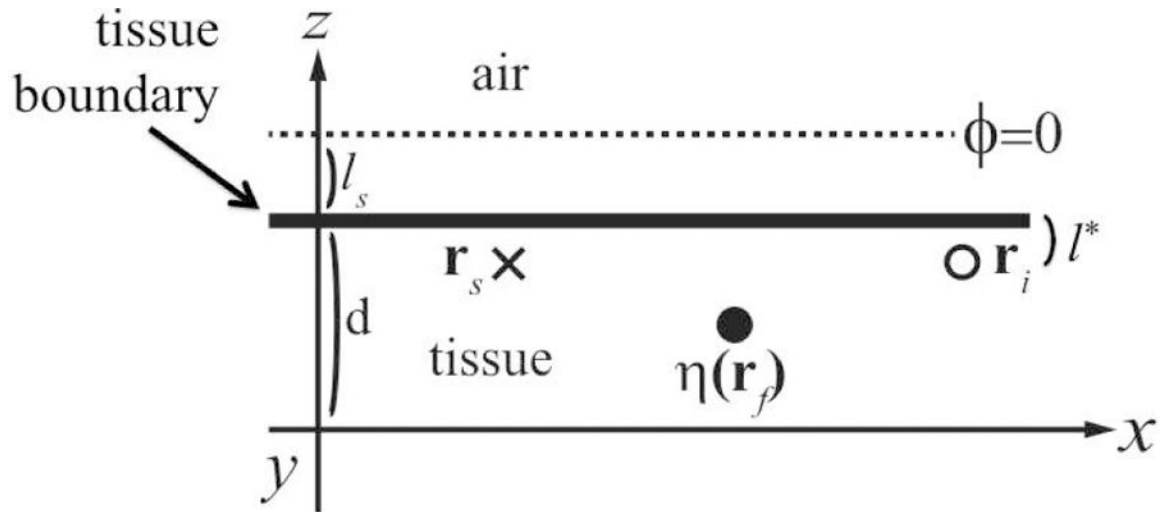
- [1]. Arridge SR and Hebden JC, "Optical imaging in medicine: Ii. modelling and reconstruction," *Phys. Med. Biol.*, vol. 42, no. 5, p. 841, 1997. [PubMed: 9172263]
- [2]. Ntziachristos V, Ripoll J, Wang LV, and Weissleder R, "Looking and listening to light: the evolution of whole-body photonic imaging," *Nat. Biotechnol.*, vol. 23, no. 3, pp. 313–320, 2005. [PubMed: 15765087]

- [3]. Huang D, Swanson EA, Lin CP, Schuman JS, Stinson WG, Chang W et al., "Optical coherence tomography," *Science*, vol. 254, no. 5035, p. 1178, 1991. [PubMed: 1957169]
- [4]. Helmchen F and Denk W, "Deep tissue two-photon microscopy," *Nat. Methods*, vol. 2, no. 12, pp. 932–940, 2005. [PubMed: 16299478]
- [5]. Davy M, Shi Z, and Genack AZ, "Focusing through random media: Eigenchannel participation number and intensity correlation," *Phys. Rev. B*, vol. 85, no. 3, p. 035105, 2012.
- [6]. Horstmeyer R, Ruan H, and Yang C, "Guidestar-assisted wavefront-shaping methods for focusing light into biological tissue," *Nat. Photon*, vol. 9, no. 9, pp. 563–571, 2015.
- [7]. Gibson A, Hebden J, and Arridge SR, "Recent advances in diffuse optical imaging," *Phys. Med. Biol*, vol. 50, no. 4, p. R1, 2005. [PubMed: 15773619]
- [8]. Ntziachristos V and Weissleder R, "Charge-coupled-device based scanner for tomography of fluorescent near-infrared probes in turbid media," *Med. Phys*, vol. 29, no. 5, pp. 803–809, 2002. [PubMed: 12033576]
- [9]. Milstein AB, Oh S, Webb KJ, Bouman CA, Zhang Q, Boas DA et al., "Fluorescence optical diffusion tomography," *Appl. Opt*, vol. 42, no. 16, pp. 3081–3094, Jun. 2003. [PubMed: 12790460]
- [10]. Corlu A, Choe R, Durduran T, Rosen MA, Schweiger M, Arridge SR et al., "Three-dimensional *in vivo* fluorescence diffuse optical tomography of breast cancer in humans," *Opt. Express*, vol. 15, no. 11, pp. 6696–6716, 2007. [PubMed: 19546980]
- [11]. Pogue BW and Paulsen KD, "High-resolution near-infrared tomographic imaging simulations of the rat cranium by use of a priori magnetic resonance imaging structural information," *Opt. Lett*, vol. 23, no. 21, pp. 1716–1718, 1998. [PubMed: 18091894]
- [12]. Ntziachristos V, Yodh A, Schnall MD, and Chance B, "MRI-guided diffuse optical spectroscopy of malignant and benign breast lesions," *Neoplasia*, vol. 4, no. 4, pp. 347–354, 2002. [PubMed: 12082551]
- [13]. Gaiend V, Tsai H-R, Webb KJ, Chelvam V, and Low PS, "Small animal optical diffusion tomography with targeted fluorescence," *J. Opt. Soc. Am. A*, vol. 30, no. 6, pp. 1146–1154, 2013.
- [14]. Tsai EHR, Bentz BZ, Chelvam V, Gaiend V, Webb KJ, and Low PS, "*In vivo* mouse fluorescence imaging for folate-targeted delivery and release kinetics," *Biomed. Opt. Express*, vol. 5, no. 8, pp. 2662–2678, 2014. [PubMed: 26236559]
- [15]. Nguyen QT, Olson ES, Aguilera TA, Jiang T, Scadeng M, Ellies LG et al., "Surgery with molecular fluorescence imaging using activatable cell-penetrating peptides decreases residual cancer and improves survival," *Proc. Natl. Acad. Sci. USA*, vol. 107, no. 9, pp. 4317–4322, 2010. [PubMed: 20160097]
- [16]. Milstein AB, Kennedy MD, Low PS, Bouman CA, and Webb KJ, "Statistical approach for detection and localization of a fluorescing mouse tumor in Intralipid," *Appl. Opt*, vol. 44, no. 12, pp. 2300–2310, 2005. [PubMed: 15861835]
- [17]. Cao G, Gaiend V, Bouman CA, and Webb KJ, "Localization of an absorbing inhomogeneity in a scattering medium in a statistical framework," *Opt. Lett*, vol. 32, no. 20, pp. 3026–3028, 2007. [PubMed: 17938688]
- [18]. Bentz BZ, Wu TC, Gaiend V, and Webb KJ, "Diffuse optical localization of blood vessels and 3D printing for guiding oral surgery," *Appl. Opt*, vol. 56, no. 23, pp. 6649–6654, 2017. [PubMed: 29047957]
- [19]. Bentz BZ, Lin D, and Webb KJ, "Superresolution diffuse optical imaging by localization of fluorescence," *Phys. Rev. Appl*, vol. 10, no. 3, p. 034021, 2018.
- [20]. Bentz BZ, Lin D, Patel JA, and Webb KJ, "Multiresolution localization with temporal scanning for super-resolution diffuse optical imaging of fluorescence," *IEEE Trans. Image Proc*, vol. 29, pp. 830–842, 2019.
- [21]. Lu Y and Low PS, "Folate-mediated delivery of macromolecular anticancer therapeutic agents," *Adv. Drug Deliv. Rev*, vol. 64, pp. 342–352, 2012.
- [22]. Kelderhouse LE, Mahalingam S, and Low PS, "Predicting response to therapy for autoimmune and inflammatory diseases using a folate receptor-targeted near-infrared fluorescent imaging agent," *Mol. Imaging Biol*, vol. 18, no. 2, pp. 201–208, 2016. [PubMed: 26242480]

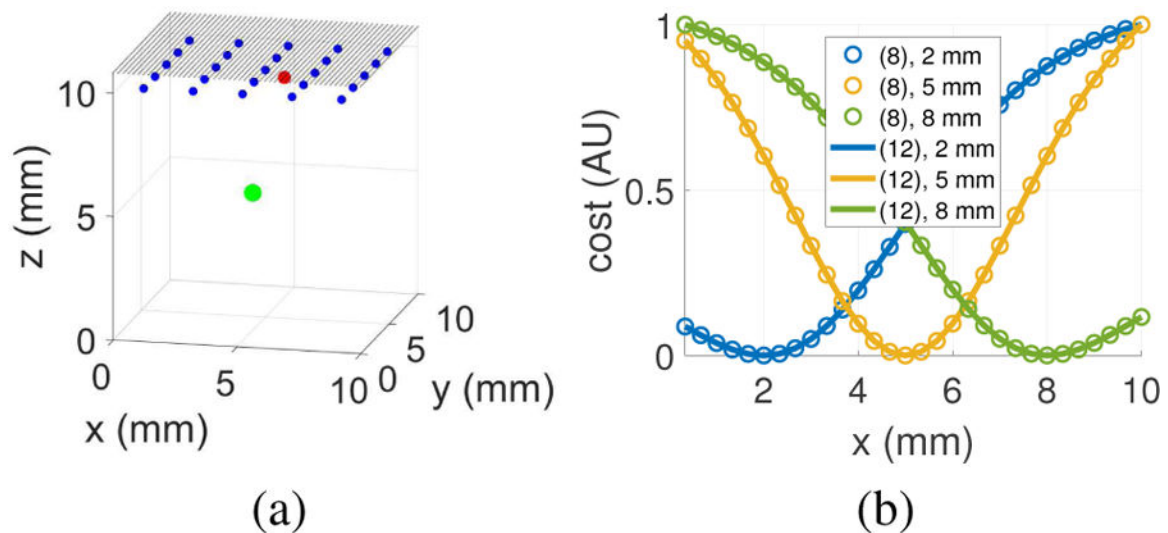


- [23]. Peelaerts W, Bousset L, Van der Perren A, Moskalyuk A, Pulizzi R, Giugliano M et al., “ $\alpha$ -synuclein strains cause distinct synucleinopathies after local and systemic administration,” *Nature*, vol. 522, no. 7556, pp. 340–344, 2015. [PubMed: 26061766]
- [24]. Yasuda R, Nimchinsky EA, Scheuss V, Pologruto TA, Oertner TG, Sabatini BL et al., “Imaging calcium concentration dynamics in small neuronal compartments,” *Sci. STKE*, vol. 2004, no. 219, p. p15, 2004. [PubMed: 14872098]
- [25]. Castanares ML, Gautam V, Drury J, Bachor H, and Daria VR, “Efficient multi-site two-photon functional imaging of neuronal circuits,” *Biomed. Opt. Express*, vol. 7, no. 12, pp. 5325–5334, 2016. [PubMed: 28018745]
- [26]. Patterson MS, Chance B, and Wilson BC, “Time resolved reflectance and transmittance for the non-invasive measurement of tissue optical properties,” *Appl. Opt.*, vol. 28, no. 12, pp. 2331–2336, 1989. [PubMed: 20555520]
- [27]. Li X, O’Leary M, Boas D, Chance B, and Yodh A, “Fluorescent diffuse photon density waves in homogeneous and heterogeneous turbid media: analytic solutions and applications,” *Appl. Opt.*, vol. 35, no. 19, pp. 3746–3758, 1996. [PubMed: 21102772]
- [28]. Arridge SR, Schweiger M, Hiraoka M, and Delpy DT, “A finite element approach for modeling photon transport in tissue,” *Med. Phys.*, vol. 20, pp. 299–309, 1993. [PubMed: 8497214]
- [29]. Schweiger M and Arridge S, “The Toast++ software suite for forward and inverse modeling in optical tomography,” *J. Biomed. Opt.*, vol. 19, no. 4, pp. 040 801–040 801, 2014.
- [30]. Ye JC, Webb KJ, Bouman CA, and Millane RP, “Optical diffusion tomography by iterative coordinate descent optimization in a Bayesian framework,” *J. Opt. Soc. Am. A*, vol. 16, no. 10, pp. 2400–2412, 10 1999.
- [31]. Bentz BZ, Bowen AG, Lin D, Ysselstein D, Huston DH, Rochet J-C et al., “Printed optics: phantoms for quantitative deep tissue fluorescence imaging,” *Opt. Lett.*, vol. 41, no. 22, pp. 5230–5233, 2016. [PubMed: 27842100]
- [32]. Bentz BZ, Chavan AV, Lin D, Tsai EH, and Webb KJ, “Fabrication and application of heterogeneous printed mouse phantoms for whole animal optical imaging,” *Appl. Opt.*, vol. 55, no. 2, pp. 280–287, 2016. [PubMed: 26835763]
- [33]. Xia W and Low PS, “Folate-targeted therapies for cancer,” *J. Med. Chem.*, vol. 53, no. 19, pp. 6811–6824, 2010. [PubMed: 20666486]
- [34]. Van Dam GM, Themelis G, Crane LM, Harlaar NJ, Pleijhuis RG, Kelder W et al., “Intraoperative tumor-specific fluorescence imaging in ovarian cancer by folate receptor- $\alpha$  targeting: first in-human results,” *Nat. Med.*, vol. 17, no. 10, pp. 1315–1319, 2011. [PubMed: 21926976]
- [35]. Paulos CM, Reddy JA, Leamon CP, Turk MJ, and Low PS, “Ligand binding and kinetics of folate receptor recycling *in vivo*: impact on receptor-mediated drug delivery,” *Mol. Pharmacol.*, vol. 66, no. 6, pp. 1406–1414, 2004. [PubMed: 15371560]
- [36]. Jacques SL, “Optical properties of biological tissues: a review,” *Phys. Med. Bio.*, vol. 58, no. 11, p. R37, 2013. [PubMed: 23666068]
- [37]. Sharma G and Martin J, “Matlab®: a language for parallel computing,” *Int. J. Parallel Program.*, vol. 37, no. 1, pp. 3–36, 2009.
- [38]. Flanagan RJ, Taylor AA, Watson ID, and Whelpton R, *Fundamentals of Analytical Toxicology*. John Wiley & Sons, 2008.
- [39]. Ye JC, Bouman CA, Webb KJ, and Millane RP, “Nonlinear multigrid algorithms for Bayesian optical diffusion tomography,” *IEEE Trans. Image Process.*, vol. 10, no. 6, pp. 909–922, 2001.
- [40]. Ancora D, Zacharopoulos A, Ripoll J, and Zacharakis G, “Fluorescence diffusion in the presence of optically clear tissues in a mouse head model,” *IEEE Trans. Med. Imag.*, vol. 36, no. 5, pp. 1086–1093, 2016.
- [41]. Ale A, Ermolayev V, Herzog E, Cohrs C, De Angelis MH, and Ntziachristos V, “FMT-XCT: *in vivo* animal studies with hybrid fluorescence molecular tomography–X-ray computed tomography,” *Nature Meth.*, vol. 9, no. 6, p. 615, 2012.
- [42]. Heijblom M, Piras D, Maartens E, Huisman EJ, van den Engh FM, Klaase JM et al., “Appearance of breast cysts in planar geometry photoacoustic mammography using 1064-nm excitation,” *J. Biomed. Opt.*, vol. 18, no. 12, p. 126009, 2013. [PubMed: 24343440]

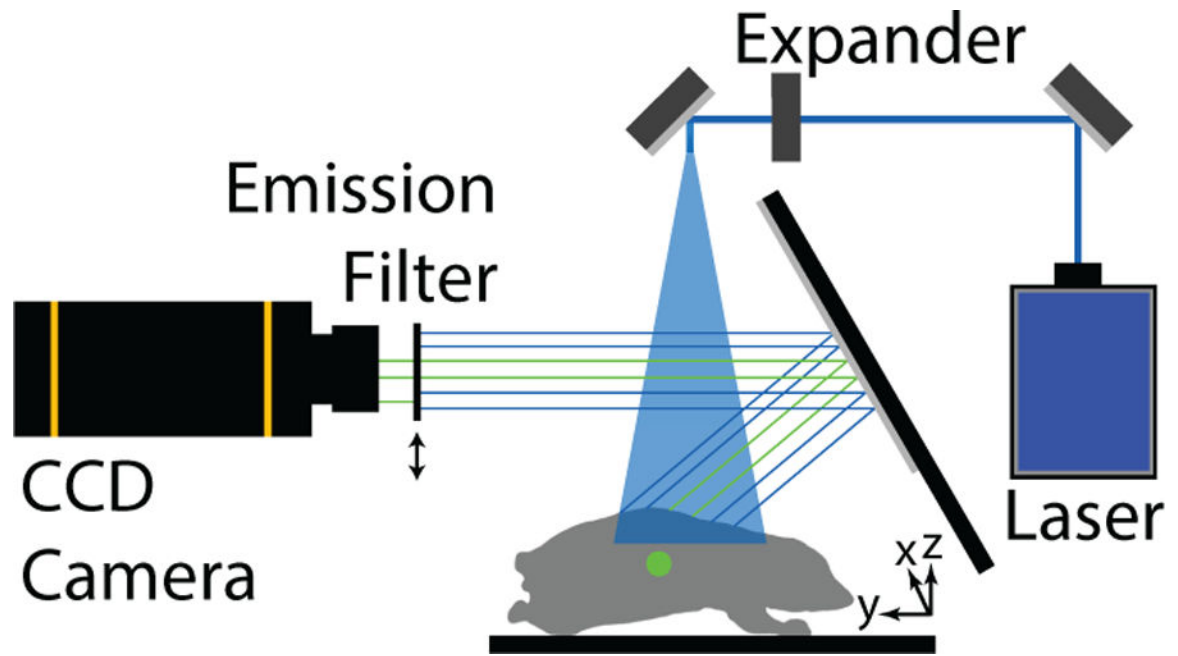
- [43]. Jewell EL, Huang JJ, Abu-Rustum NR, Gardner GJ, Brown CL, Sonoda Y et al., "Detection of sentinel lymph nodes in minimally invasive surgery using indocyanine green and near-infrared fluorescence imaging for uterine and cervical malignancies," *Gynecol. Oncol.*, vol. 133, no. 2, pp. 274–277, 2014. [PubMed: 24582865]
- [44]. Chen F, Brown GM, and Song M, "Overview of three-dimensional shape measurement using optical methods," *Opt. Eng.*, vol. 39, no. 1, pp. 10–22, 2000.
- [45]. Koo EH, Lansbury PT, and Kelly JW, "Amyloid diseases: abnormal protein aggregation in neurodegeneration," *Proc. Nat. Acad. Sci.*, vol. 96, no. 18, pp. 9989–9990, 1999. [PubMed: 10468546]
- [46]. Rochet J-C, Outeiro TF, Conway KA, Ding TT, Volles MJ, Lashuel HA et al., "Interactions among  $\alpha$ -synuclein, dopamine, and biomembranes," *J. Mol. Neurosci.*, vol. 23, no. 1–2, pp. 23–33, 2004. [PubMed: 15126689]
- [47]. Kaminski Schierle GS, Bertoncini CW, Chan FT, van der Goot AT, Schwedler S, Skepper J et al., "A FRET sensor for non-invasive imaging of amyloid formation *in vivo*," *ChemPhysChem*, vol. 12, no. 3, pp. 673–680, 2011. [PubMed: 21308945]
- [48]. Gaiand V, Webb KJ, Kularatne S, and Bouman CA, "Towards *in vivo* imaging of intramolecular fluorescence resonance energy transfer parameters," *JOSA A*, vol. 26, no. 8, pp. 1805–1813, 2009. [PubMed: 19649115]
- [49]. Cannon JR, Sew T, Montero L, Burton EA, and Greenamyre JT, "Pseudotype-dependent lentiviral transduction of astrocytes or neurons in the rat substantia nigra," *Exp. Neurol.*, vol. 228, no. 1, pp. 41–52, 2011. [PubMed: 21056560]
- [50]. Bullmore E and Sporns O, "Complex brain networks: graph theoretical analysis of structural and functional systems," *Nature Rev. Neurosci.*, vol. 10, no. 3, pp. 186–198, 2009. [PubMed: 19190637]
- [51]. Ogawa S, Lee TM, Kay AR, and Tank DW, "Brain magnetic resonance imaging with contrast dependent on blood oxygenation," *Proc. Nation. Acad. Sci.*, vol. 87, no. 24, pp. 9868–9872, 1990.

**Fig. 1:**

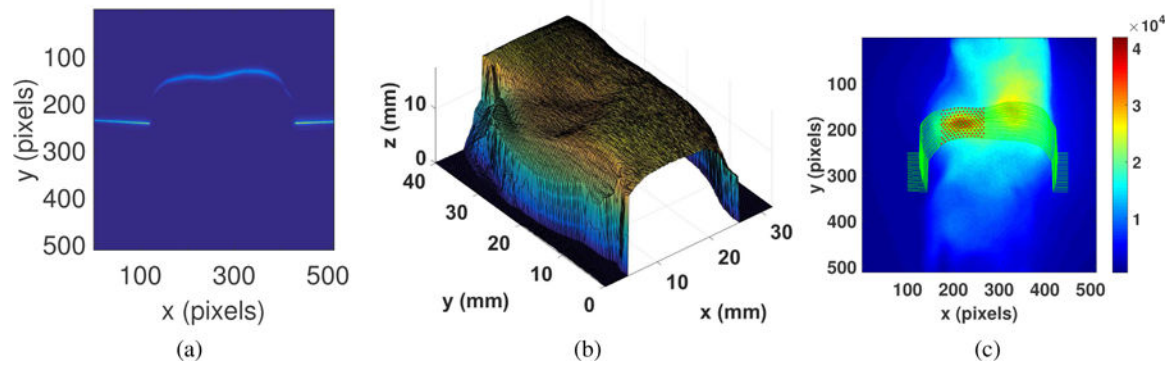
Model geometry for a single tissue boundary, where  $\mathbf{r} = (x, y, z)$  and the  $y$ -axis is going into the page. The tissue thickness  $d$  is assumed large. An excitation source (X) at  $\mathbf{r}_s$  scattering length  $l^* = 3D$  away from the tissue boundary, as and a fluorescence emission detector (O) at  $\mathbf{r}_i$  are placed one shown. A fluorescence inhomogeneity (●) is at the unknown position  $\mathbf{r}_f$ . A zero flux ( $\phi = 0$ ) boundary condition is assumed at a distance  $l_s = 5.03D$  above the physical boundary to simulate a semi-infinite planar geometry [16], [19].

**Fig. 2:**

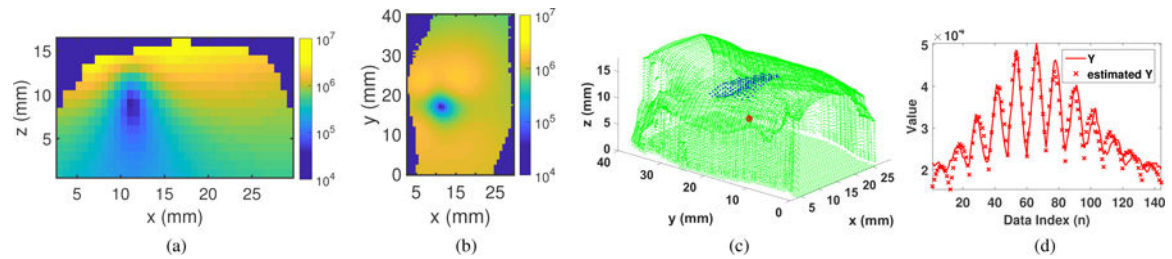
Simulation demonstrating the localization of a fluorescent inhomogeneity. (a) Simulation geometry, where 25 detectors (blue) and 1 excitation source (red) are placed at the  $z = 10$  mm plane. A fluorescent point source (green) is located at  $\mathbf{r}_f = (x_f, y_f, z_f) = (5.0, 5.0, 5.0)$  mm. The tissue boundary is the gray shaded region, and the simulated source and detectors are  $P^*$  below the surface. The tissue optical parameters are  $\mu'_s = 2.0 \text{ mm}^{-1}$ ,  $\mu_a = 0.025 \text{ mm}^{-1}$ , and the refractive index is 1.33. Fluorescence emission data measured at the detectors is used to localize the inhomogeneity. (b) Cost functions calculated as a function of position,  $x$ , for  $x_f = 2, 5$ , and  $8$  mm, as indicated by the legend, and fixed  $y_f = 5.0$  mm and  $z_f = 5.0$  mm. The circular markers signify cost calculations using (8), and the solid lines signify cost calculations using (12). The excitation source in (a) is used to calculate (8) but not (12). For each value of  $x_f$ , (8) and (12) are matched and minimized at the true value. In 3D, the cost is calculated at each  $x$ ,  $y$ , and  $z$  coordinate position within the region of interest.



**Fig. 3:**  
 Experimental setup for the localization of a fluorescent inhomogeneity (green point). The laser source is tuned to  $\lambda_x$ , and the beam is expanded by a lens to illuminate the sample. Detection is by a CCD camera with a bandpass emission filter centered at  $\lambda_m$ .

**Fig. 4:**

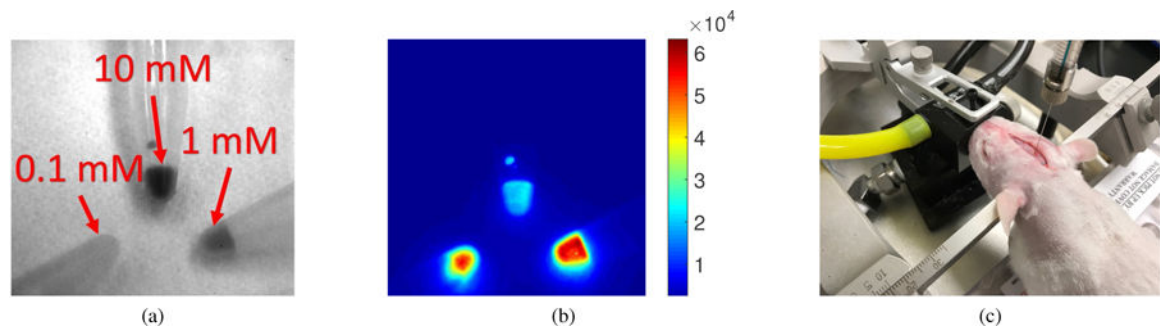
Data captured for localization. (a) CCD images for a single laser line scan. The line was moved along the  $y$  direction, and 92 CCD images were captured and used to generate the 3D profile shown in (b). This profile defines the geometry of the problem. The head of the mouse is at  $y < 0$  mm. (c) The fluorescence CCD image captured through the band pass filter. Peaks in fluorescence due to a tumor and a kidney are visible. The colorbar shows fluorescence intensity. The 144 detectors are plotted as red points, and the 3D laser line scans used to determine the position in mm of these detectors are plotted in green.



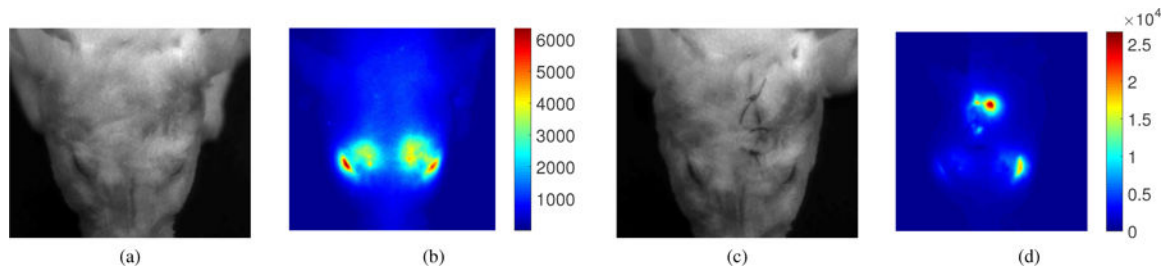
**Fig. 5:**

Localization of a fluorescent mouse tumor using the data from Fig. 4. The 3D profile was discretized into 62,574 nodes, and the cost was calculated at each node position. (a) Cost image slice at  $y = 17$  mm. (b) Cost image slice at  $z = 9$  mm. The position that minimized the cost, or the estimated position of the tumor, was (11.1, 17.0, 9.0) mm, and is the point with minimum cost in (a) and (b). There is less contrast in the cost with depth, as seen in (a), because the detectors are only on the top surface. (c) Plot of the boundary nodes in green, the simulated detector positions in blue, and the estimated tumor position in red. (d) Comparison of the measured data (y) and the forward model (estimated y) using the estimated optical properties and tumor position. Since the surface is slowly varying, and only one inhomogeneity dominates the contribution to the data at the detectors, the model fits the data well. The discrepancy could be due to autofluorescence or fluorescence from the kidney.



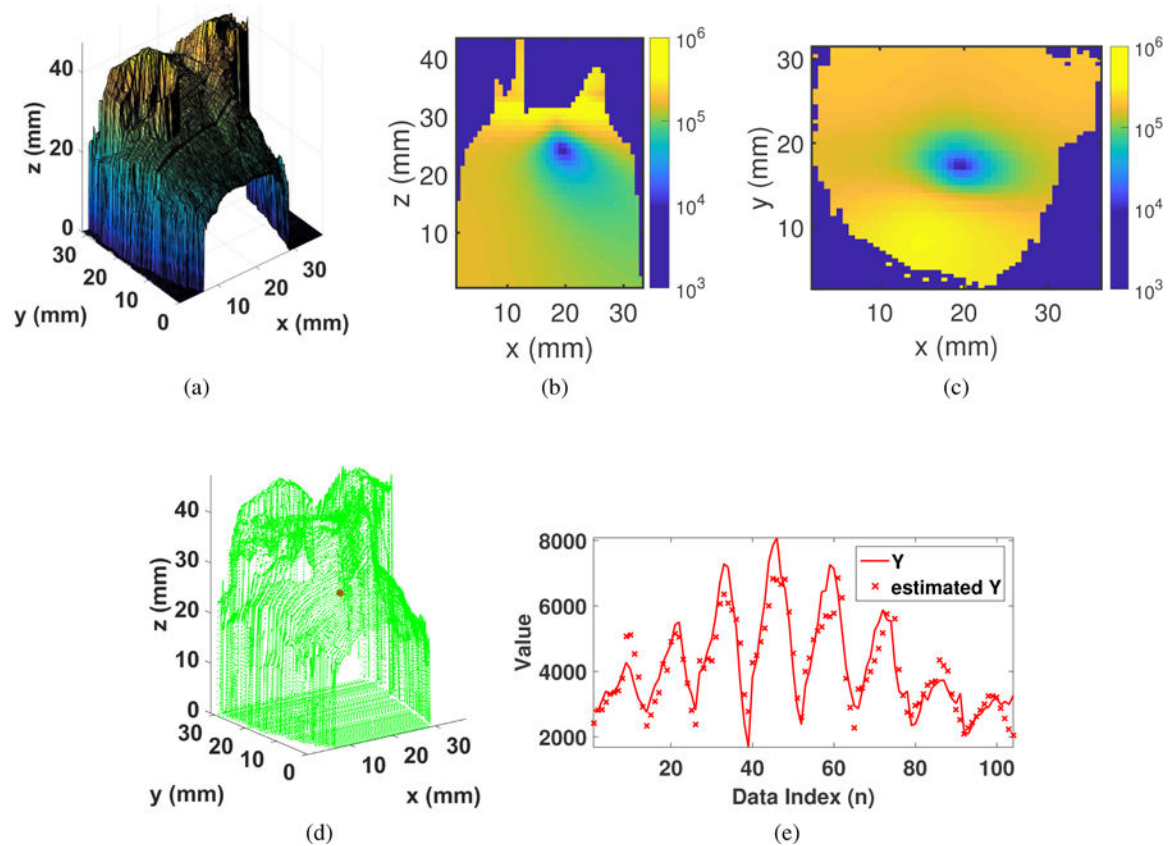
**Fig. 6:**

Preparation of ATTO647N and stereotaxic injection through the skull into a dead rat. (a) CCD image of 10, 1, and 0.1 mM solutions of ATTO647N in DMSO that were prepared from a stock solution. (b) CCD fluorescence image of the ATTO647N from (a). A strong quenching of the ATTO647N at high concentration is apparent, limiting the concentration that should be injected for maximum signal. (c)  $2\ \mu\text{L}$  of the 1 mM solution of ATTO647N in PBS was injected into the rat *substantia nigra*. The injection coordinates were 5 mm anterior-posterior, 2 mm left-right from the Bregma, and 8 mm dorsal-ventral from the skull surface.



**Fig. 7:**

Rat fluorescence before and after stereotaxic injection of ATTO647N 8 mm below the skull surface. (a) CCD image under room light before injection. (b) CCD fluorescence image through the bandpass filter before injection. There is strong autofluorescence present. (c) CCD image under room light after injection. The surgical sutures are visible. (d) CCD fluorescence image through the bandpass filter after injection. A signal from the region of the injection site is clearly visible, despite the autofluorescent background.

**Fig. 8:**

Localization of ATTO647N using data from Fig. 6. (a) 3D profile generated using the laser line scan of the rat. Along the  $y$ -axis, the rat eyes are at about  $y = 0$  mm, and the ears are between about  $y = 20$  mm and  $y = 30$  mm. The 3D profile was discretized into 124,047 nodes, and the cost was calculated at each node position. (b) Cost image slice at  $y = 16.6$  mm. (c) Cost image slice at  $z = 24$  mm. The position with minimum cost, or the estimated position of the ATTO647N, is (19.8, 16.6, 24.0) mm. The estimated depth of the ATTO647N is about 8.3 mm below the tissue surface, in excellent agreement with the injection site 8 mm below the skull surface. (d) Plot of the boundary nodes in green and the estimated position. (e) Comparison of the measured data ( $y$ ) and the forward model (estimated  $y$ ) using the estimated tissue parameters and the estimated position of the ATTO647N. The surface is not as slowly varying as that of Fig 4, and there is significant autofluorescence, causing errors in the fit. However, it was still possible to estimate the correct position of the ATTO647N.